ORIGINAL ARTICLE

A voxelized model of direct infusion into the corpus callosum and hippocampus of the rat brain: model development and parameter analysis

Jung Hwan Kim · Thomas H. Mareci · Malisa Sarntinoranont

Abstract Recent experimental studies have shown convective-enhanced delivery (CED) to be useful for transporting macromolecular therapeutic agents over large tissue volumes in the central nervous system (CNS). There are limited tools currently available for predicting tissue distributions in the brain. We have developed a voxelized modeling methodology in which CNS tissues are modeled as porous media, and transport properties and anatomical boundaries are determined semi-automatically on a voxel-by-voxel basis using diffusion tensor imaging (DTI). By using this methodology, 3D extracellular transport models of the rat brain were developed. Macromolecular tracer distributions following CED in two different infusion sites (corpus callosum and hippocampus) were predicted. Sensitivity of models to changes in infusion parameters, transport properties, and modeling parameters was determined. Predicted tracer distributions were most sensitive to changes in segmentation threshold, DTI resolution, tissue porosity, and infusion site. This DTI-based voxelized modeling methodology provides a potentially rapid means of estimating CED transport.

Keywords Convective-enhanced delivery (CED) ·
Diffusion tensor imaging (DTI) · Computational model ·
Anisotropic extracellular transport · Central nervous
system (CNS) · Intraparenchymal infusion

J. H. Kim · M. Sarntinoranont (✉)
Department of Mechanical and Aerospace Engineering,
University of Florida, 212 MAE-A, 116250, Gainesville,
FL 32611-6250, USA
e-mail: msarnt@ufl.edu

T. H. Mareci
Department of Biochemistry and Molecular Biology,
University of Florida, Gainesville, FL 32611, USA

1 Introduction

Despite the high therapeutic potential of many macromolecular drugs, the delivery of macromolecular agents to targeted tissues for treatment of cancer and other degenerative diseases of the central nervous system (CNS) remains challenging [10]. One barrier to the systemic administration of macromolecules is low capillary permeability, i.e., the blood–brain barrier. Even if agents overcome this barrier, extracellular (interstitial) tissue transport is limited due to low diffusivity, as well as, degradation and binding of the macromolecules in tissue. One promising technique to surmount these barriers uses direct infusion in to tissue, i.e., convection-enhanced delivery (CED), to supplement diffusion and increase the distribution of large molecules through convective extracellular transport [7, 24, 45].

In this study, CED transport models were developed for two brain regions: the corpus callosum and hippocampus. The corpus callosum may provide an ideal site for targeting large volumes of the brain since white matter tracts extend over significant regions of the brain. Also, recent studies indicate the potential usefulness of hippocampal infusions for treating epilepsy and other neurological disorders [17, 46]. Previous CED transport studies have been conducted for these brain regions, and tracer distribution studies show extracellular transport in white matter to be dependent on the orientation of the white matter tracts, such that preferential transport occurs within the extracellular space parallel to axonal fibers [7, 23, 36]. For example, Geer and Grossman found albumin-Evans blue tracer to transport extensive distances along white matter tracts following infusions into the rat corpus callosum [13]. Distributions following hippocampal CED of particular therapeutic agents including galanin and musimol have also been investigated by Schött et al. [39] and Heiss et al. [15].

Computational models of the brain that predict CED flow patterns and spatial drug distributions would be useful in treatment optimization and planning. Previous transport models of CED and drug release have been developed for nervous tissue using porous media assumptions [2, 3, 8, 18, 26–29, 40]. The majority of these studies apply isotropic and homogeneous tissue transport assumptions. However, to predict distributions for large infusion volumes, transport models should incorporate tissue boundaries and anisotropic tissue properties that account for the underlying fibrous structure of white matter tissues. Anisotropic CNS transport models are just beginning to be developed [21, 35, 38] and use diffusion tensor imaging (DTI) data to assign spatially varying tissue properties. For DTI, the self-diffusion of water molecules in tissue is represented on a voxel-by-voxel basis as a rank-2 tensor. This water diffusion tensor provides a description of the averaged three-dimensional translational self-diffusion (in units of cm^2/s). Anisotropy in this diffusivity measurement results from restricted water movement in the underlying structure averaged over a large number of fibers and combines information from both the extracellular and intracellular spaces. Preferential directions of water diffusion have been found to correspond to the average aligned fiber directions within a voxel, and these data have been used to calculate fiber-tract trajectories within fibrous tissues [4, 6, 9, 25, 32]. For CNS transport models, averaged tissue alignment data from DTI has been used to assign preferential extracellular transport directions [21, 35, 38].

In the development of computational brain models, there is also a need for efficient and time-saving modeling techniques. Geometric reconstruction and meshing of tissue volumes is often the most time-consuming and labor intensive leg of computational model development, especially for the brain with its complex boundaries. Such slice-by-slice segmentation and tissue volume reconstruction procedures have been previously implemented by our group and others in previous CED CNS transport models [22, 38, 41]. Recently, we have implemented a DTI-based voxelized modeling technique that provides more rapid estimates of tissue transport. Tissue alignment data from DTI is used for tissue segmentation and to assign preferential transport properties on a semi-automatic, voxel-by-voxel basis. Spatially varying tissue properties are then incorporated into computational (finite volume) porous media models to predict flow and transport in tissues. We have tested this methodology for CED within the rat spinal cord [19] using T2-weighted signal intensity in the absence of diffusion-weighting for tissue segmentation. Predicted spinal cord tracer distributions correlated well with non-voxelized models [38] and experimental distribution measures by Wood et al. [45] for small infusion volumes.

In this study, the voxelized modeling methodology was adapted for CED into the brain. The embedded and convoluted nature of white matter tracts within the brain provides a more challenging transport problem. In these cases, segmentation of white and gray matter tissue boundaries was based on the extent of water diffusion anisotropy as determined from DTI data. A computational transport model for the rat brain was developed and used to determine 3D extracellular transport fields for velocity and pressure, as well as, the distribution of a macromolecular tracer, albumin, during CED in the corpus callosum in the frontal lobe and the ventral hippocampus. A parametric analysis was completed for the CED infusion model, and sensitivity of predicted transport to varying infusion parameters (infusion site and rate), tissue properties (porosity and transport properties), and computational parameters (tissue segmentation and voxel resolution) was determined. Sensitivity of predicted transport to low rates of endogenous flow from metabolism and capillary leakage was also considered.

2 Methods

2.1 Diffusion tensor imaging

Use of excised, fixed tissue in DTI scans allowed for the long scan times necessary to obtain high resolution microstructural information of the rat brain. Surgery was conducted in accordance with the NIH guidelines on the use of animals in research and the regulations of the Animal Care and Use Committee of the University of Florida. Once anesthetized, rats were exsanguinated then perfusion fixed with a 4% solution of paraformaldehyde in phosphate buffered saline (PBS). After overnight fixation, the brain was removed and stored in the fixative solution. Before imaging, the tissue was soaked overnight in PBS to remove the fixative. The rat brain was imaged in fluorinated oil, and DTI data sets were obtained using a 17.6 T magnet.

Multiple-slice images, weighted by water translational diffusion, were measured (~ 11 h) using a spin-echo pulse sequence. Measurements were performed with recovery time of 1,400 ms, and echo time of 28 ms. The diffusion-weighted images were acquired with a field of view 30 mm $\times$ 15 mm in a matrix of 200 $\times$ 100 in 32 slices of 0.3 mm thickness. This is a resolution of 150 μm $\times$ 150 μm $\times$ 300 μm. Images with low diffusion-weighting (100 s/mm^2) and high diffusion-weighting (1,250 s/mm^2) were measured with 5 averages in 6 gradient-directions and 46 gradient-directions, respectively, specified by the tessellations of an icosahedron on the unit hemisphere.

Diffusion-weighted images were interpolated (bilinear interpolation with nearest neighbor sampling) by a factor of two in the slice direction (data matrix of 200 $\times$ 100 $\times$ 64). After initial image processing, the multiple-slice DTI data

was fit to a rank-2 tensor model of water translational diffusion, $\mathbf{D_e}$, using multiple-linear regression [5]. The effect of gradient cross-terms was included in the calculation of the diffusion tensor. The diffusion tensor, the T2-weighted signal intensity in the absence of diffusion-weighted gradients (S_o), and fractional anisotropy (FA) which is a scalar measure of anisotropy were calculated using previously published methods [4, 5].

2.2 Tissue segmentation

A semi-automatic methodology was implemented to reconstruct a three-dimensional rectangular tissue volume with regions delineated for isotropic gray matter and anisotropic white matter and ventricle spaces (free water). FA values from the DTI data set were used to differentiate between voxels of different tissues and free water regions. FA is a convenient measure since anisotropy of the water diffusion tensor varies with the extent of tissue alignment within the image voxel. Therefore, regions of aligned axons within white matter tissues have higher FA values than within gray matter regions which consist primarily of non-aligned cell bodies. Ranges of FA threshold values were adjusted, using visualization software (Amira v.4.1, TGS, San Diego, CA), until selected tissue regions matched with anatomical boundaries for white matter, gray matter, and ventricle spaces in a rat brain atlas [31]. Ranges of FA specified in Table 1 were used to assign tissue properties in the computational transport model using a custom Matlab (Matlab v. 7.3.0, Mathworks, Natick, MA) subroutine, see Fig. 1. FA threshold values for white matter were found to correspond to previously measured ranges [20].

2.3 Extracellular transport model

2.3.1 Theory

Nervous tissue was assumed to be a rigid porous medium. This assumption is valid for low rates of infusion where tissue pressures remain low. The continuity equation is

$$\nabla \cdot \mathbf{v} = \beta \tag{2}$$

where $\mathbf{v}$ is the tissue-averaged extracellular fluid velocity, β is the volumetric flow rate source term for extracellular fluid, i.e., endogenous flow sources for metabolism and microvasculature (No fluid sink term is included because there are no lymphatic in brain tissues) [1, 11, 14]. Darcy's law been widely used in the analysis of extracellular flow within tissues. This empirical relation governs flow through porous media

$$\mathbf{v} = -\mathbf{K} \cdot \nabla p \tag{3}$$

Table 1 (A) Tissue properties used in the extracellular transport simulations. (B) Fractional anisotropy (FA) ranges used in tissue segmentation of the rat brain

Parameters	Values	References
(A)		
ϕ	0.26	[37, 45]
D_{tgm}	1.60×10^{-7} cm^2/s	[42]
$D_{twm\parallel}$	2.29×10^{-7} cm^2/s	[34, 42]
$D_{twm\perp}$	1.34×10^{-7} cm^2/s	[34, 42]
D_{csf}	1.34×10^{-7} cm^2/s	[34, 42]
$K_{wm\parallel}$	6.75×10^{-9} cm^4/dyne-s	[38]
$K_{wm\perp}$	4.22×10^{-10} cm^4/dyne-s	[38]
K_{gm}	4.22×10^{-12} cm^4/dyne-s	[38]

Brain region	FA range
(B)	
White matter	$0.275 \leq \text{FA} \leq 1$
Gray matter	$0.1 \leq \text{FA} < 0.275$
CSF	$0 \leq \text{FA} < 0.1$

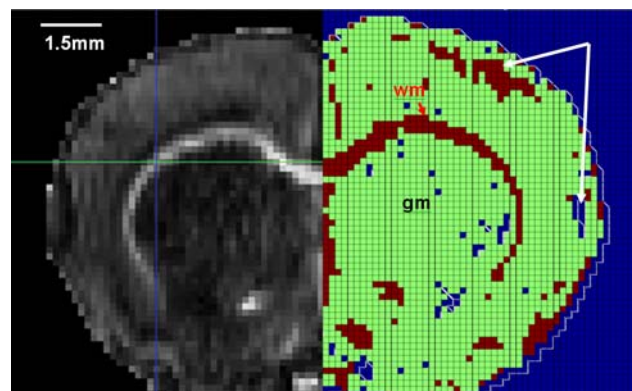*wm* white matter, *gm* gray matter, *CSF* cerebrospinal fluid

Fig. 1 Tissue segmentation of the rat brain using DTI-derived FA: (*left*) FA map of the coronal plane; (*right*) corresponding tissue segmentation map of a reflected image (*green*: gray matter, *red*: white matter, *blue*: free-water region). In FA images, white corresponds to FA = 1 and black corresponds to FA = 0. *Solid arrows* point to artifact voxels. *Colored lines* correspond to planes intersecting the point of infusion within the corpus callosum. (Color figure online)

where p is the pore fluid pressure, and $\mathbf{K}$ is the hydraulic conductivity tensor which is dependent on the pore geometry, fluid viscosity, and underlying tissue structure. Darcy's law was also applied to CSF regions instead of the Newtonian constitutive equation since the effects of external viscous flows on transport within brain tissues were assumed to be small.

Albumin is a non-binding and non-reacting macromolecule that is commonly used as an extracellular tracer in distribution studies. By assuming no tissue sources or sinks for this molecule (e.g., binding or metabolism), transport

through tissue was governed by convection (advection) and diffusion

$$\frac{\partial c}{\partial t} + \nabla \cdot \left(\frac{\mathbf{v}c}{\phi}\right) = \nabla \cdot (\mathbf{D_t} \cdot \nabla c) \qquad (4)$$

where t and ϕ are time and tissue porosity, respectively. c is the averaged concentration with respect to tissue volume. $\mathbf{D_t}$ is the diffusivity tensor of the macromolecule in the tissue. Concentration was solved in terms of the normalized variable.

$$\tilde{c} = \frac{c}{c_i\phi} \qquad (5)$$

where c_i is the infusate concentration.

2.3.2 Extracellular transport tensors

Bulk porous media transport properties of hydraulic conductivity, $\mathbf{K}$, and tracer diffusivity, $\mathbf{D_t}$, for gray matter tissue and CSF were considered to be isotropic. In white matter, each nodal point in the computational mesh was assigned spatially varying, anisotropic $\mathbf{K}$ and $\mathbf{D_t}$ tensors using preferential transport directions extracted from $\mathbf{D_e}$, with $\mathbf{K}$ and $\mathbf{D_t}$ tensors assumed to share the same maximum eigenvector (direction of maximum transport) as $\mathbf{D_e}$ [43]. It should be noted that $\mathbf{D_e}$ was measured over a sufficient voxel volume such that water diffusion over a number of fibers was averaged to provide directional transport information for bundles of fibers. $\mathbf{K}$ and $\mathbf{D_t}$ tensors for each nodal point were assigned using the relationships shown below [38].

$$\mathbf{K} = \mathbf{V} \begin{bmatrix} K_\perp & 0 & 0 \\ 0 & K_\perp & 0 \\ 0 & 0 & K_\| \end{bmatrix} \mathbf{V^T} \qquad (6a)$$

$$\mathbf{D_t} = \mathbf{V} \begin{bmatrix} D_\perp & 0 & 0 \\ 0 & D_\perp & 0 \\ 0 & 0 & D_\| \end{bmatrix} \mathbf{V^T} \text{ where } \mathbf{V} = [\mathbf{v_1 v_2 v_3}] \qquad (6b)$$

$\mathbf{v_i}$ are the unit eigenvectors of $\mathbf{D_e}$ ordered according to the eigenvalues of $\mathbf{D_e}$ such that $\mathbf{v_3}$ is the unit eigenvector corresponding to the largest eigenvalue. Tensor eigenvalues ($K_\perp$, $K_\|$, $D_\perp$, and $D_\|$) correspond to transport magnitudes in directions perpendicular and parallel to aligned fiber directions and were determined from literature, Table 1. The baseline value assigned to CSF hydraulic conductivity was taken to be approximately three orders of magnitude higher than that of gray matter to reflect less resistance to flow.

2.3.3 Computational model

For the 3D transport models, two rectangular volumes covering portions of the rat brain were created using

meshing software (GAMBIT v.2.4.6, Fluent, Lebanon, NH). Meshed tissue volumes were 9 mm × 7.5 mm × 9.45 mm for the corpus callosum region and 12 mm × 7.35 mm × 9.45 mm for the hippocampal region. Eight-node brick elements were used, and each mesh element corresponded to an interpolated image voxel element (150 μm × 150 μm × 150 μm) from DTI data. A user-defined function was utilized to assign tensor transport properties for $\mathbf{K}$ and $\mathbf{D_t}$ at each nodal point using the DTI-based segmentation results of the previous section. Additionally, cube-shaped infusion sites corresponding to the outer diameter of a 31 gauge needle (150 μm × 150 μm × 150 μm) were placed in the middle of the tissue volumes according to the following approximate stereotactic coordinates: bregma 0.72 mm anterior, 3.75 mm lateral, 3.6 mm deep within the corpus callosum and bregma −6.00 mm anterior, 5.00 mm lateral, 5.00 mm deep within the hippocampus. A constant infusion rate of 0.3 μL/min, similar to that used in the Greer and Grossman study [13], was simulated at these sites.

Equations 2–4 were solved within the computational fluid dynamic software package, FLUENT (v. 6.3.26, Fluent, Lebanon, NH) using a control-volume-based technique. To solve for porous media transport, the conservation of momentum equation for a fluid was replaced with Darcy's law, as described in [38], by introducing a momentum source term corresponding to Darcy's law ($-K^{-1} v$). However, a convective acceleration term was still in place, and for Darcy's law to hold, convective accelerations which are dependent on velocity and velocity gradients were assumed to be negligible. (In our simulations, convective accelerations within highest velocity regions were found to be approximately 10 orders of magnitude lower than the momentum source term corresponding to Darcy's law.) A user-defined subroutine was also created to assign the tracer diffusion tensor components at each node point. Transient concentration profiles were solved using steady-state velocities solutions. (To check this assumption, concentration simulations using steady state velocity profiles were compared to concentration simulations using transient velocities. Steady-state flow conditions were established after <1 s and predicted tracer distribution volumes were changed by <0.001% which we assumed to be negligible).

It was also assumed that external boundaries were a sufficiently long distance from the infusion site such that flows or variations in pressure at these boundaries did not have a significant effect in the region of interest, and, $p = 0$ was assigned at all outer boundaries. For concentration simulations, $\tilde{c}$ was set to the maximum normalized value ($\tilde{c} = 1$) at the infusion site boundary, and $\tilde{c} = 0$ at outer boundaries. Initial conditions for albumin transport assumed no tracer in the tissue, $\tilde{c} = 0$, at time zero.

2.3.4 Parameter analysis

Baseline tissue properties are listed in Table 1. In all parameter studies, final tissue distribution volumes for 5.1 μL tracer infusions were compared. These tissue distributions volumes were calculated by adding together voxels that exceeded a threshold value of ∼5% of maximum concentration.

Computational modeling parameters of interest included the FA thresholds used for segmentation and the voxel resolution of DTI data sets. FA thresholds used for white matter segmentation were varied over three different ranges: 0.275–1.0 (baseline), 0.30–1.0, and 0.34–1.0. FA ranges of 0.30–1.0 and 0.34–1.0 slightly underestimated white matter regions, Fig. 2a–d. To quantify sensitivity, changes in the segmented white matter volumes within virtual cubes (4.49 mm^3) surrounding the infusion sites were calculated. The effect of varying image resolution was also considered, and the high-resolution DTI data set was resampled at lower resolutions. However, at low voxel resolutions of 600 μm × 600 μm × 600 μm, difficulties were encountered in obtaining segmentation maps that were representative of the selected rat brain structures with major features of the corpus callosum, internal capsule, and hippocampus (i.e., granular layer of dentate gyrus and CA3) being lost. As a result, only data resampled at an 300 μm × 300 μm × 300 μm resolution was used to generate transport models with coarser meshes, Fig. 2e, f. The effect of varying FA threshold values on the lower resolution data set was also compared, and predicted tracer distributions for two different FA threshold values (0.275–1.0 and 0.29–1.0) for white matter segmentation were compared.

Parametric studies looking at the effects of changing tissue properties varied tissue porosity (0.22, 0.26, 0.30), the ratio of the hydraulic conductivity parallel to the fiber tracts to the conductivity perpendicular to fiber tracts ($K_\parallel/K_\perp = 16$ and 24), and the ratio of white matter to gray matter hydraulic conductivity ($K_{wm}/K_{gm} = 50$, 100, and 150 where K_{wm} is the hydraulic conductivity perpendicular to the fiber tracts). These tissue property ranges were selected based on a previous parameter analysis of a spinal cord CED model [38].

The sensitivity of CED transport to infusion conditions was also determined. Sensitivity to cannula placement within a specific brain structure was determined by comparing two additional infusion locations within the ventral hippocampus: 0.15 mm medial and 0.15 mm directly below the original hippocampal infusion site in the coronal plane. Also, three different infusion rates (0.1, 0.3, 0.5 μL/min) were simulated. The effect of endogenous fluid flow on CED transport was also considered.
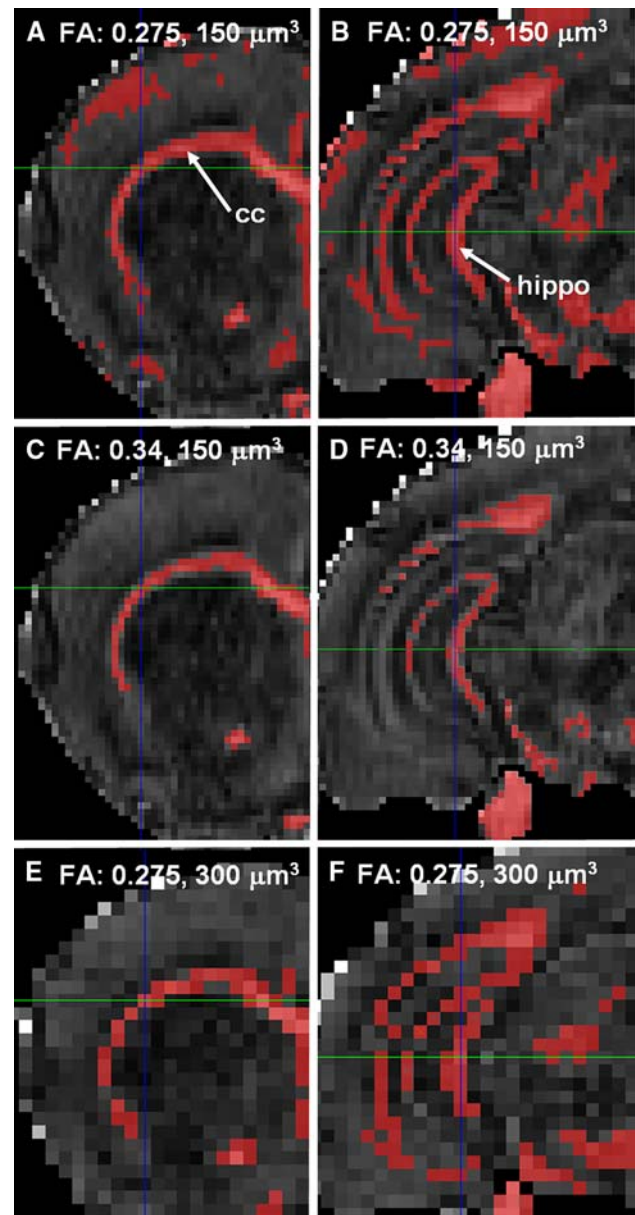

Fig. 2 Variation in segmented white matter regions (*red*) within the corpus callosum (*right column*) and hippocampus (*left column*) for different FA threshold values and DTI voxel resolutions. (**a**, **b**) white matter range of 0.275 < FA < 1.0 and voxel resolution = 150 μm^3; (**c**, **d**) white matter range of 0.34 < FA < 1.0 and voxel resolution = 150 μm^3; and (**e**, **f**) white matter range of 0.275 < FA < 1.0 and voxel resolution = 300 μm^3. Segmented regions are superimposed on coronal FA maps. *Arrows* in **a** and **b** point to white matter regions within the corpus callosum (cc) and hippocampus (hippo). (Color figure online)

For these cases, a fluid mass generation term corresponding to fluid sources from capillaries, microvasculature, and active secretion by the cerebral endothelium was applied uniformly in all tissue regions (0.1–0.3 μL/min g as estimated by Abbott [1]).

3 Results

3.1 Diffusion tensor imaging

For the fixed rat brain, the $\mathbf{D_e}$ data set was measured and corresponding eigenvectors and fractional anisotropy values were calculated for each voxel. Calculated fractional anisotropy image for a coronal slice is shown in Fig. 1. High resolution FA images clearly delineate white matter regions (lighter voxels), as well as, the surrounding gray matter tissue and other free-water regions (darker voxels) of the exterior and ventricles. A segmentation map is also presented in Fig. 1. A small volume of artifact voxels were noted consisting of isolated white matter-labeled voxels in gray matter and isolated gray matter-labeled voxels in white matter. These appear to be a result of locally high or low values of FA and reflect local tissue structure variation. In order to determine the extent of these artifacts, the total volume of these voxels was estimated. For each DT imaging slice, regions of varying tissue composition were color coded, and artifact voxels were noted by eye by comparing with an anatomical atlas [31]. Total artifact voxel volumes were estimated to be ∼8% of the total tissue volume.

3.2 Extracellular flow

Steady-state extracellular fluid flow fields were predicted for 0.3 μL/min infusions into the corpus callosum and hippocampus, Fig. 3. Simulated flow was directed outwardly from the infusion site with highest velocities ($\sim 1.96 \times 10^{-5}$ m/s in the corpus callosum and $\sim 1.99 \times 10^{-5}$ m/s in hippocampus) and highest pressures ($\sim 2.01 \times 10^5$ dyne/cm^2 in the corpus callosum and $\sim 3.57 \times 10^5$ dyne/cm^2 in the hippocampus) adjacent to the infusion site. For corpus callosum CED, preferential fluid flow was found along white matter tracts, and fluid velocities in white matter injection regions were two orders of magnitude greater than in neighboring gray matter, Fig. 3a. These flow patterns were as expected since white matter tissues have more conducive fluid transport properties than gray matter. For hippocampal

CED, the predicted highest velocity flows were also confined within white matter, Fig. 3b. However, a more convoluted fluid flow pattern was predicted since the hippocampus has a more complicated structure consisting of layers of white matter (i.e., molecular and pyramidal cell layers) and gray matter (granular cell layers).

3.3 Albumin transport

Corpus callosum and hippocampus CED models showed different tracer distribution patterns due to differing tissue structures. Predicted albumin distributions for corpus callosum CED are shown in Fig. 4 for infusions up to 4.5 μL. Preferential spread of albumin was along the direction of the structured white matter tracts as shown in the FA map of Fig. 1. Spatial distribution profiles showed relatively flat concentration profiles with steep concentration drops at the advancing front. At the final simulated infusion time ($t = 17$ min; 5.1 μL total infusion volume; not shown), the albumin tracer was predicted to penetrate less than 1 mm into adjacent gray matter regions. Tracer distributions for hippocampal CED are shown in Fig. 5. Tracers were predicted to distribute rapidly within white matter regions, most likely along granule cell dendrites (mossy fibers and pyramidal cells) in the molecular layer of the dentate gyrus in the ventral hippocampus, and then spread throughout interspersed gray matter Within this hippocampal model, tracer volumes within gray matter hippocampal regions were found to be larger than within white matter hippocampal regions. Overall, albumin tracer was predicted to penetrate greater distances into gray matter compared to the predicted penetration within the corpus callosum, Fig. 6. In both models, a linear relationship was predicted between total infusion volumes and total tissue distribution volumes over the range of infusion volumes studied, <5.1 μL, Fig. 6. Albumin tracer was also predicted to spread into ventricle CSF regions once a threshold infusion volume was reached (∼0.3 μL). For the chosen infusion sites, the volume of tracer entering CSF regions was minimal compared with the total distribution volumes simulated.

Fig. 3 Predicted velocity contours for infusions into the **a** corpus callosum and **b** hippocampus in coronal planes. **c** Peclet number contour map for hippocampal infusion (coronal plane). CED infusion rate was 0.3 μL/min. Contours are overlaid on corresponding FA images (*white* corresponds to FA = 1 and *black* corresponds to FA = 0)
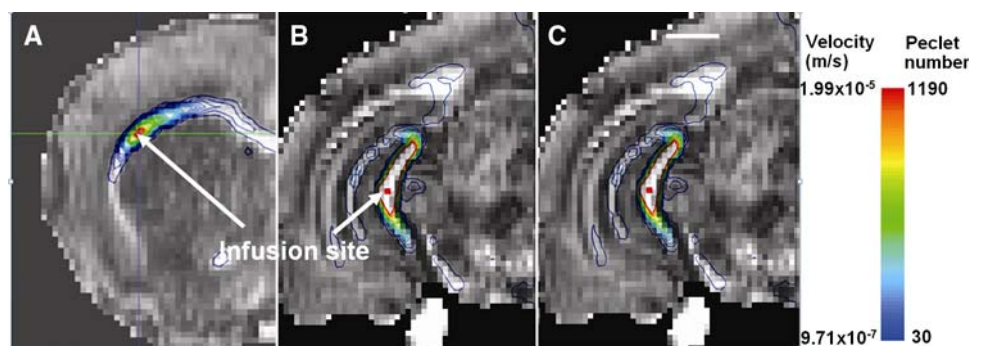
Fig. 4 Predicted albumin distributions during infusion into the corpus callosum in coronal planes. Tracer distributions at increasing times **a** 5 min, **b** 10 min, and **c** 15 min are shown. CED infusion rate was 0.3 µL/min. Concentration contours are normalized and overlaid on corresponding FA images (*white* corresponds to FA = 1 and *black* corresponds to FA = 0)
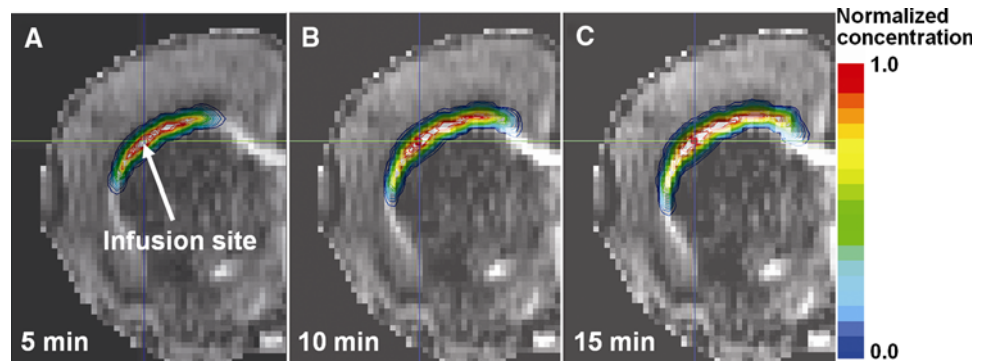

Fig. 5 Predicted albumin distributions during infusion into the hippocampus in coronal planes. Tracer distributions at increasing times **a** 5 min, **b** 10 min, and **d** 15 min are shown. CED infusion rate was 0.3 µL/min. Concentration contours are normalized and overlaid on corresponding FA images (*white* corresponds to FA = 1 and *black* corresponds to FA = 0)
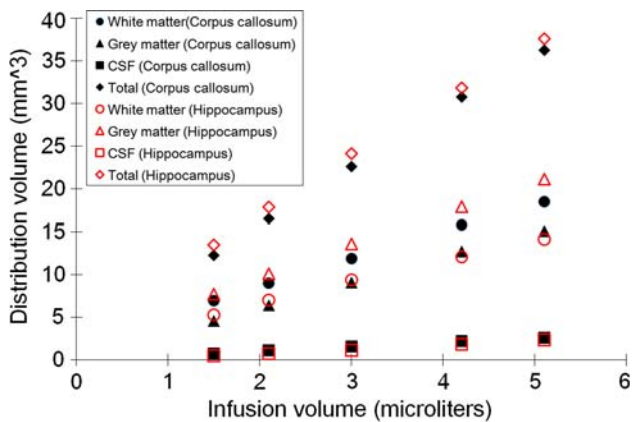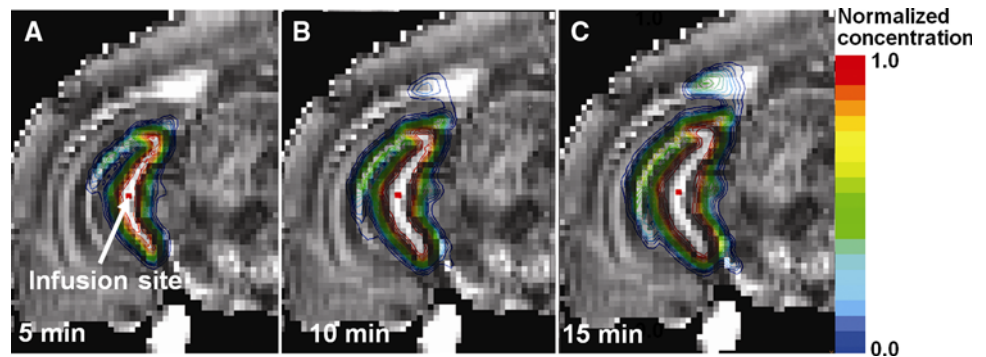

Fig. 6 Predicted tissue distribution volumes for albumin tracer in white matter, gray matter, and CSF for CED (0.3 µL/min) in the hippocampus and corpus callosum

The Peclet number, which represents the ratio of mass transport by convection to diffusion, is defined as $Pe = vl/D$ where v is the velocity magnitude, l is a typical length scale (=1 mm), and D is the tracer diffusivity coefficient (1.67×10^{-7} cm^2/s) [38]. The maximum Peclet numbers (1.18×10^3 for corpus callosum CED and 1.19×10^3 for hippocampal CED) were determined to be adjacent to the infusion site, and Pe was found to decrease proportionally with velocity magnitude and distance from the infusion site, Fig. 3c. Convection-dominated transport regions

($Pe \gg 1$) estimated using Pe values of 30 were found to extend significant distances from the point of infusion and corresponded to white matter and adjacent tissue regions.

3.4 Computational model parameter analysis

3.4.1 Tissue segmentation

By increasing the FA threshold value from 0.275 to 0.34, segmented white matter volumes were decreased by 28% in the corpus callosum model with minimal effect on the connectivity of the fiber structure. Segmented white matter volumes in the hippocampus model decreased by a greater amount, 54%, and there was significant loss of connectivity of white matter structures. This disproportionate change is due to the fact that FA values within fiber tract regions of the corpus callosum were relatively higher resulting in less sensitivity to FA changes. Correspondingly, predicted tracer distributions in the corpus callosum were changed <1% by changes in FA thresholds, Fig. 7a. In the hippocampus, predicted tracer distributions were minimally effected changing the FA threshold from 0.275 to 0.3. However, increasing the threshold to 0.34 resulted in an ~10% decrease in the predicted distribution volume after 5.1 µL infusion, Fig. 7b, since connectivity within the white matter structures was lost.

Fig. 7 Sensitivity of predicted tracer distribution volumes in the corpus callosum (*left column*) and hippocampus (*right column*) to varying (**a, b**) FA threshold values, (**c, d**) DTI voxel resolution, and (**e, f**) tissue porosity. Baseline tissue properties used in simulations: $K_{\parallel}/K_{\perp} = 16$, $K_{wm}/K_{gm} = 100$, and infusion rate $= 0.3\ \mu L/min$
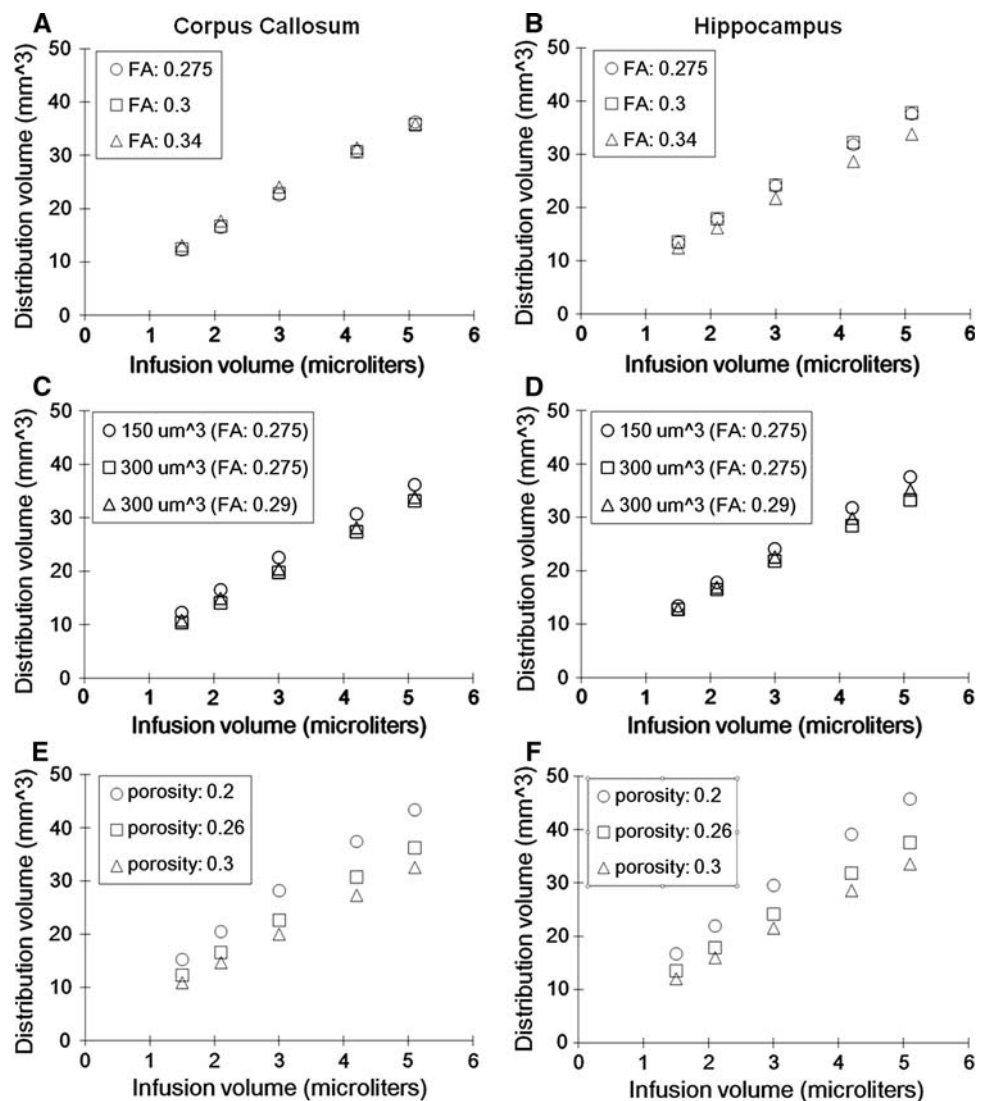
3.4.2 Voxel resolution

Convective-enhanced delivery simulations using lower resolution voxels ($300\ \mu m^3$) resulted in 6.5 and 6.7% decreases in final tracer distribution volumes within the hippocampus and corpus callosum, respectively, after $5.1\ \mu L$ infusions, Fig. 7c, d. The larger voxel size resulted in a loss of structural information and connectivity of finer white matter structures was again lost within the hippocampus. The effect of varying the segmentation threshold at this lower resolution was also considered. Predicted tracer distribution volumes within the hippocampus and corpus callosum increased by 11 and 2% when the FA threshold was varied between 0.275 and 0.29. Overall increases in tracer distributions were likely due to changes in tissue boundaries with grid coarsening. By comparing with results at the higher resolution, predicted distributions were more sensitive to changes in FA threshold values at lower resolutions.

3.5 Infusion parameter analysis

3.5.1 Tissue transport properties

The effect of varying tissue porosity (0.2, 0.26, and 0.3) on final tracer distribution volumes is shown in Fig. 7e, f. As expected, lower tissue porosities resulted in greater tracer distributions for the same infusion volume, and tracer distribution volumes varied approximately inversely with porosity. Tissue transport parameter analyses for $K_{\parallel}/K_{\perp}$ and K_{wm}/K_{gm} ratios were also conducted (not shown). Final albumin tissue distribution volumes were changed less than $\sim 0.4\%$ (hippocampus) and $\sim 0.1\%$ (corpus callosum) when the white matter $K_{\parallel}/K_{\perp}$ ratio was varied between 16 and 24. Relative changes between white and gray matter transport properties, i.e., the K_{wm}/K_{gm} ratio, were found to affect the predicted albumin distribution volumes to some extent. Increasing the K_{wm}/K_{gm} ratio from 50 to 150 resulted in ~ 5 and $\sim 7\%$ increases in tracer tissue volumes

within the hippocampus and corpus callosum after 5.1 μL infusions.

3.5.2 Infusion site

Sensitivity of CED transport to small changes in infusion location (0.15 mm medial and 0.15 mm below the selected infusion site; not shown) was determined in the hippocampal model. Infusion into an adjacent gray matter (rather than white matter) region resulted in increased infusion pressure $(7.05 \times 10^5$ dyne/cm$^2)$ as well as velocity $(3.74 \times 10^{-5}$ m/s). Predicted tracer distribution volumes were found to change less than ~1% for the range of infusion volumes studied. The effect of different infusion flow rates on distribution volumes was also simulated. Due to the rigid pore assumption of our model, predicted albumin distribution volumes were increased only by 1.6% when the infusion rate was changed from 0.1 to 0.5 μL/min.

The effect of endogenous fluid flow on CED transport in the corpus callosum and hippocampus was also considered. The resulting CED tracer distribution volumes changed less than ~1% over the CED infusion period for the endogenous flow rates investigated.

4 Discussion

The voxelized modeling approach of this study utilizes DTI data to assign tissue boundaries, transport properties, and preferential transport directions within 3D brain transport models. This methodology relies on minimal user input and provides a relatively rapid process when compared with previous manual image segmentation and volume meshing processes used for constructing models of the brain with its complex white matter structures. By using this technique, tissue transport models for the rat corpus callosum and hippocampus were developed, and estimates of extracellular pressure, extracellular velocity fields, and tracer transport were predicted. The high resolution DTI data obtained from a fixed brain provided sufficient mesh resolution for rapidly converging transport predictions. In parametric analyses, predicted CED tracer transport was stable over the variable ranges tested, and CED tracer distributions were most sensitive to changes in FA thresholds used for segmentation, DTI voxel resolution, tissue porosity, and infusion site. To a lesser extent, predicted distributions were also sensitive to relative differences in gray matter and white matter transport properties.

For CED into the corpus callosum, the computational model predicted preferential tracer transport along white matter tracts in the medial–lateral direction with limited penetration into adjacent gray matter. Significant tracer

spread in the white matter is consistent with experimental observations by Greer and Grossman [13] following infusions into the corpus callosum and experimental observations by Prabhu et al. [33] for infusions into the putamen. In the hippocampus, previous researchers have investigated the therapeutic response of compounds following CED [15, 39, 46]; however, corresponding distribution studies in the hippocampus are sparse and difficult to compare.

Differences in CED transport between the two brain sites were determined by comparing tracer distribution volumes and infusion pressures. Tracer distribution volumes in the hippocampus were predicted to be greater in gray matter than in white matter; whereas, tracer infusions into the corpus callosum followed the opposite trend. These distributions may be explained by differences in aligned tissue structures and tissue composition between the two infusion sites. At the hippocampal infusion site, there is a relatively smaller volume of white matter (likely corresponding to aligned mossy fibers extending from granule cell layers). Once white matter tissue is filled, tracer must be transported into the surrounding gray matter. Gray matter penetration may also be facilitated by the greater cell connectivity between the layers of white and gray matter within this region which was reflected in the underlying fiber structure. With CED into the corpus callosum, tracers preferentially distribute within the relatively larger white matter structure before transporting into adjacent tissues, resulting in a greater ratio of white matter spread. Also, since gray matter has lower hydraulic conductivity (greater resistance to fluid flow) than white matter, infusion pressures at the hippocampal site were predicted to be higher than for the corpus callosum where the infusion site was embedded in a larger volume of white matter.

Convective-enhanced delivery transport predictions were found to be sensitive to tissue segmentation parameters. Varying the FA range used for white matter segmentation changed the tissue composition within models and the hippocampus model was more sensitive to changes in FA thresholds. Location-dependent sensitivity is likely due to differing tissue composition; the corpus callosum consists primarily of bundles of mylenated axons with strong alignment and greater tissue density, whereas, the hippocampus has more varied neuronal tissue and a less dense structure that results in weaker alignment [12]. Spatial variation of FA within differing brain regions has been previously reported by Le Bihan [20]. In addition, it should be noted that CSF regions were not always correctly assigned using this FA-based segmentation approach. Assigned ventricle regions did not completely match those of the brain atlas [31]. This may have lead to some error of tissue distributions near ventricle regions. However, loss of tracer into adjacent ventricle regions was found to be small

for the selected infusion sites. Artifact voxels as described in the "Results" section were also introduced with FA-based segmentation. Tracer predictions were found to be insensitive to the presence of these voxels with no concentration jumps found near infusion sites due to the fact that total artifact voxel volumes were a small percentage of the total model volumes. Increasing the number of these voxels will lead to variation in concentration and pressure profiles. For example, our voxelized spinal cord models predicted comparable distribution volumes to those measured experimentally, but concentration profiles were less uniform in the vicinity of artifact voxels [38]. These artifact voxels are likely due to local tissue structure variations, e.g., crossing fibers, or maybe due to other imaging limitations, e.g., edge boundary effects. Methods to account for the effects of fiber crossings in the DTI data set may further reduce the incidence of these voxels [16, 30, 44].

Model predictions were also found to be sensitive to the DTI resolution. Simulations that resampled the DTI data at lower resolutions predicted tracer distribution volumes to decrease. This is likely due a partial voxel volume effect since the entire volume of all voxels under the concentration threshold were added together to calculate distribution volumes. Thus, it is possible that at the lower resolutions used in in vivo studies, voxelized transport models will underestimate CED tissue distributions depending on the choice of the concentration threshold value. Also, distribution patterns will likely change with spatial averaging and fine transport pathways within complex fiber regions may be lost. Care must be taken when determining if DTI data sets possess sufficient resolution to capture underlying transport characteristics. Future studies will focus on validating this modeling method using lower resolution DTI data sets obtained in vivo.

After varying tissue transport properties, CED transport was predicted to be most sensitive to changes in tissue porosity with lower porosities resulting in greater tracer spread. This trend was expected since a smaller fluid volume per unit tissue volume results in greater pore-level velocity. Thus, tracer convection was inversely proportional to tissue porosity. Porosity values were estimated from previous experimental CNS studies for normal and edematous states but were not measured at the specific brain regions used in this study. Given the sensitivity of the models to this parameter, additional measures of porosity, especially under CED conditions, are necessary. Varying the white matter $K_{\parallel}/K_{\perp}$ ratio was found to have only a small effect on predicted tracer distribution volumes. Transport sensitivity to hydraulic conductivity anisotropy was found to be less than in our previous spinal cord CED model [38] in which white matter was adjacent to CSF. In the brain, the different embedded nature of the white matter

tracts provides a significant difference since flow from white matter is primarily distributed into adjacent gray matter and not into CSF. CED transport was slightly more sensitive to relative changes in white and gray matter transport properties, K_{wm}/K_{gm}. Fluid velocities in white matter increased with increases in K_{wm}/K_{gm}, and convective tracer transport was enhanced in these regions.

Changes in cannula placement and infusion rates within the same brain structure were also investigated. Tracer distribution patterns and tissue volumes were minimally affected by small changes in location. However, significant changes in infusion pressure were predicted depending on if the cannula was placed within either white or gray matter. Again, higher infusion pressures were predicted in gray matter due to its lower hydraulic conductivity. These results suggest that pressure-induced effects including fluid efflux or tissue damage may vary with cannula location. Varying infusion rates did not affect predicted tracer distribution volumes. This result was expected for the rigid porous media model since transport properties did not change with flow rate or pressure.

Also, endogenous flows over a range of flow rates that have been previously estimated from literature by Abbott (0.1–0.3 μL/min g [1]) were predicted to minimally effect tracer distributions during the course of CED infusions. The effect of this underlying tissue flow on tracer transport was expected to be small over short time scales. The effect of such flows over longer time periods following CED may be more substantial, e.g., affecting tracer clearance, since endogenous flows will continue to spread tracer after the end of infusion.

In this study, limitations of using fixed tissues are associated with changes due to tissue shrinkage with fixation or expansion due to infusion in tissue during CED. With uniform shrinkage, fiber orientation is not expected to change, and FA fields are not expected to significantly change. Also, CSF regions surrounding the brain were overestimated since the skull region was not included in the fixed tissue scans. However, dilution of tracer in CSF likely has a small effect on internal tissue distributions, which are dominated by transport that occurs primarily in one direction, from the tissue into the CSF.

In this study, a methodology for incorporating DTI data to rapidly develop extracellular transport models of the brain is presented. The developed computational models provide useful insight into the effects of underlying transport forces and tissue structure on local CED transport. To advance these models, improved segmentation schemes may be incorporated and additional measures of tissue porosity should be measured given the shown sensitivity of model results to segmentation and porosity. Also, further experimental CED and DTI imaging studies are needed to test this modeling approach in vivo. It should be noted that

while high field magnets and long imaging times were required to develop these models for the small animal rat brain, similar DTI methods have been developed for clinical use. These methods allow fast data measurement at a resolution on a human scale [20] that captures the structural features similar to the resolution on the size scale used in this study. Thus, with further development, these image-based models may eventually be used as surgical tools to guide CED.

References

1. Abbott NJ (2004) Evidence for bulk flow of brain interstitial fluid: significance for physiology and pathology. Neurochem Int 45:545–552

2. Barry SI, Aldis GK (1992) Flow-induced deformation from pressurized cavities in absorbing porous tissues. Bull Math Biol 54:977–997

3. Basser PJ (1992) Interstitial pressure, volume, and flow during Infusion into brain-tissue. Microvasc Res 44:143–165

4. Basser PJ, Jones DK (2002) Diffusion-tensor MRI: theory, experimental design and data analysis—a technical review. NMR Biomed 15:456–467

5. Basser PJ, Mattiello J, Lebihan D (1994) MR diffusion tensor spectroscopy and imaging. Biophys J 66:259–267

6. Basser PJ, Pajevic S, Pierpaoli C, Duda J, Aldroubi A (2000) In vivo fiber tractography using DT-MRI data. Magn Reson Med 44:625–632

7. Bobo RH, Laske DW, Akbasak A, Morrison PF, Dedrick RL, Oldfield EH (1994) Convection-enhanced delivery of macromolecules in the brain. Proc Natl Acad Sci USA 91:2076–2080

8. Chen ZJ, Broaddus WC, Viswanathan RR, Raghavan R, Gillies GT (2002) Intraparenchymal drug delivery via positive-pressure infusion: experimental and modeling studies of poroelasticity in brain phantom gels. IEEE Trans Biomed Eng 49:85–96

9. Conturo TE, Lori NF, Cull TS, Akbudak E, Snyder AZ, Shimony JS, Mckinstry RC, Burton H, Raichle ME (1999) Tracking neuronal fiber pathways in the living human brain. Proc Natl Acad Sci USA 96:10422–10427

10. De Boer G, Gaillard PJ (2007) Drug targeting to the brain. Annu Rev Pharmacol Toxicol 47:323–355

11. Dykstra KH, Hsiao JK, Morrison PF, Bungay PM, Mefford IN, Scully MM, Dedrick RL (1992) Quantitative examination of tissue concentration profiles associated with microdialsis. J Neurochem 58:931–940

12. Freund TF, Buzsaki G (1996) Interneurons of the hippocampus. Hippocampus 6:347–470

13. Geer CP, Grossman SA (1997) Interstitial fluid flow along white matter tracts: a potentially important mechanism for the dissemination of primary brain tumors. J Neuro Oncol 32:193–201

14. Haraldsson B (1986) Physiological-studies of macromolecular transport across capillary walls—studies on continuous capillaries in rat skeletal-muscle. Acta Physiol Scand 128:1–40

15. Heiss JD, Walbridge S, Morrison P, Hampton RR, Sato S, Vortmeyer A, Butman JA, O'malley J, Vidwan P, Dedrick RL, Oldfield EH (2005) Local distribution and toxicity of prolonged hippocampal infusion of muscimol. J Neurosurg 103:1035–1045

16. Hess CP, Mukherjee P, Han ET, Xu D, Vigneron DB (2006) Q-ball reconstruction of multimodal fiber orientations using the spherical harmonic basis. Magn Reson Med 56:104–117

17. Hrabetova S (2005) Extracellular diffusion is fast and isotropic in the stratum radiatum of hippocampal CA1 region in rat brain slices. Hippocampus 15:441–450

18. Kalyanasundaram S, Calhoun VD, Leong KW (1997) A finite element model for predicting the distribution of drugs delivered intracranially to the brain. Am J Physiol 273:R1810–R1821

19. Kim JH, Astary GW, Chen X, Mareci TH, Sarntinoranont M (2009) Voxelized model of interstitial transport in the rat spinal cord following direct infusion into white matter. J Biomech Eng T ASME 131:071007

20. Le Bihan D, Mangin JF, Poupon C, Clark CA, Pappata S, Molko N, Chabriat H (2001) Diffusion tensor imaging: concepts and applications. J Magn Reson Imaging 13:534–546

21. Linninger A, Somayaji MR, Erickson T, Guo XD, Penn RD (2008) Computational methods for predicting drug transport in anisotropic and heterogeneous brain tissue. J Biomech 41:2176–2187

22. Linninger A, Somayaji MR, Mekarski M, Zhang LB (2008) Prediction of convection-enhanced drug delivery to the human brain. J Theor Biol 250:125–138

23. Lonser RR, Gogate N, Morrison PF, Wood JD, Oldfield EH (1998) Direct convective delivery of macromolecules to the spinal cord. J Neurosurg 89:616–622

24. Lonser RR, Walbridge S, Garmestani K, Butman JA, Walters HA, Vortmeyer O, Morrison PF, Brechbiel MW, Oldfield EH (2002) Successful and safe perfusion of the primate brainstem: in vivo magnetic resonance imaging of macromolecular distribution during infusion. J Neurosurg 97:905–913

25. Mori S, Kaufmann WE, Pearlson GD, Crain BJ, Stieltjes B, Solaiyappan M, Van Zijl P (2000) In vivo visualization of human neural pathways by magnetic resonance imaging. Ann Neurol 47:412–414

26. Morrison PF, Laske DW, Bobo H, Oldfield EH, Dedrick RL (1994) High-flow microinfusion—tissue penetration and pharmacodynamics. Am J Physiol 266:R292–R305

27. Morrison PF, Chen MY, Chadwick RS, Lonser RR, Oldfield EH (1999) Focal delivery during direct infusion to brain: role of flow rate, catheter diameter, and tissue mechanics. Am J Physiol 277:R1218–R1229

28. Neeves KB, Lo CT, Foley CP, Saltzman WM, Olbricht WL (2006) Fabrication and characterization of microfluidic probes for convection enhanced drug delivery. J Control Release 111:252–262

29. Netti PA, Travascio F, Jain RK (2003) Coupled macromolecular transport and gel mechanics: poroviscoelastic approach. Aiche J 49:1580–1596

30. Ozarslan E, Shepherd TM, Vemuri BC, Blackband SJ, Mareci TH (2006) Resolution of complex tissue microarchitecture using the diffusion orientation transform (DOT). NeuroImage 31:1086–1103

31. Paxinos G, Watson C (1998) The rat brain in stereotatic coordinate. Elsevier Academy Press, Burlington, MA

32. Poupon C, Mangin JF, Clark CA, Frouin V, Regis J, Le Bihan D, Bloch I (2001) Towards inference of human brain connectivity from MR diffusion tensor data. Med Image Anal 5:1–15

33. Prabhu SS, Broaddus WC, Gillies GT, Loudon WG, Chen ZJ, Smith B (1998) Distribution of macromolecular dyes in brain

using positive pressure infusion: a model for direct controlled delivery of therapeutic agents. Surg Neurol 50:367–375

34. Prokopova S, Vargova L, Sykova E (1997) Heterogeneous and anisotropic diffusion in the developing rat spinal cord. Neuro-Report 8:3527–3532

35. Raghavan R, Brady ML, Rodriguez-Ponce MI, Hartlep A, Pedain C, Sampson JH (2006) Convection-enhanced delivery of therapeutics for brain disease, and its optimization. Neurosurg Focus 20:E12

36. Reulen HJ, Graham R, Spatz M, Klatzo I (1977) Role of pressure-gradients and bulk flow in dynamics of vasogenic brain edema. J Neurosurg 46:24–35

37. Sarntinoranont M, Banerjee RK, Lonser RR, Morrison PF (2003) A computational model of direct interstitial infusion of macro-molecules into the spinal cord. Ann Biomed Eng 31:448–461

38. Sarntinoranont M, Chen XM, Zhang B, Mareci TH (2006) Computational model of interstitial transport in the spinal cord using diffusion tensor imaging. Ann Biomed Eng 34:1304–1321

39. Schott PA, Bjelke B, Ogren SO (1998) Distribution and kinetics of galanin infused into the ventral hippocampus of the rat: rela-tionship to spatial learning. Neuroscience 83:123–136

40. Smith JH, Humphrey JC (2007) Interstitial transport and trans-vascular fluid exchange during infusion into brain and tumor tissue. Microvasc Res 73:58–73

41. Somayaji MR, Xenos M, Zhang L, Mekarski M, Linninger A (2008) Systematic design of drug delivery therapies. Comput Chem Eng 32:89–98

42. Tao L, Nicholson C (1996) Diffusion of albumins in rat cortical slices and relevance to volume transmission. Neuroscience 75:839–847

43. Tuch DS, Wedeen VJ, Dale AM, George JS, Belliveau JW (2001) Conductivity tensor mapping of the human brain using diffusion tensor MRI. Proc Natl Acad Sci USA 98:11697–11701

44. Tuch DS, Reese TG, Wiegell MR, Makris N, Belliveau JW, Wedeen VJ (2002) High angular resolution diffusion imaging reveals intravoxel white matter fiber heterogeneity. Magn Reson Med 48:577–582

45. Wood JD, Lonser RR, Gogate N, Morrison PF, Oldfield EH (1999) Convective delivery of macromolecules into the naive and traumatized spinal cords of rats. J Neurosurg 90:115–120

46. Zhung WN, Bast T, Feldon J (2002) Effects of hippocampal N-methyl-D-aspartate infusion on locomotor activity and prepulse inhibition: differences between the dorsal and ventral hippo-campus. Behav Neurosci 116:72–84